



# Unconventional superconductivity in Cr-based compound $\text{Pr}_3\text{Cr}_{10-x}\text{N}_{11}$



C. S. Chen<sup>1</sup>, Q. Wu<sup>1</sup>, M. Y. Zou<sup>1</sup>, Z. H. Zhu<sup>1</sup>, Y. X. Yang<sup>1</sup>, C. Tan<sup>1</sup>, A. D. Hillier<sup>2</sup>, J. Chang<sup>3</sup>, J. L. Luo<sup>4,5,6</sup>, W. Wu<sup>4,5</sup> ✉ & L. Shu<sup>1,7,8</sup> ✉

We report results of specific heat and muon spin relaxation ( $\mu\text{SR}$ ) measurements on a polycrystalline sample of  $\text{Pr}_3\text{Cr}_{10-x}\text{N}_{11}$ , which shows superconducting state below  $T_c = 5.25$  K, a large upper critical field  $H_{c2} \sim 20$  T and a residual Sommerfeld coefficient  $\gamma_0$ . The field dependence of  $\gamma_0(H)$  resembles  $\gamma$  of the U-based superconductors  $\text{UTe}_2$  and  $\text{URhGe}$  at low temperatures. The temperature-dependent superfluid density measured by transverse-field  $\mu\text{SR}$  experiments is consistent with a  $p$ -wave pairing symmetry. ZF- $\mu\text{SR}$  experiment suggests a time-reversal symmetry broken superconducting transition, and temperature-independent spin fluctuations at low temperatures are revealed by LF- $\mu\text{SR}$  experiments. These results indicate that  $\text{Pr}_3\text{Cr}_{10-x}\text{N}_{11}$  is a candidate of  $p$ -wave superconductor which breaks time-reversal symmetry.

Spin-triplet superconductivity is rich in physics compared to conventional spin-singlet superconductivity due to the orbital and spin degrees of freedom, and it also has potential application in quantum computation<sup>1,2</sup>. Therefore, experimental verification of spin-triplet superconductivity has been a long-sought goal. However, intrinsic spin-triplet superconductors are rare. The candidates, such as  $\text{Sr}_2\text{RuO}_4$ <sup>3–12</sup> and  $\text{UPt}_3$ <sup>13–17</sup>, are still in controversy. Recently, unconventional superconductivity was discovered in  $\text{UTe}_2$ <sup>18,19</sup>. The exotic behaviors, including the coexistence of magnetic fluctuations and superconductivity, point nodes in the superconducting energy gap structure<sup>20–23</sup>, and time-reversal symmetry breaking inferred from observations of a spontaneous Kerr response in the superconducting state<sup>24,25</sup>, all point to an odd-parity, spin-triplet pairing superconducting state. The mechanism of spin-triplet pairing is much less understood than that of its counterpart spin-singlet pairing explained by the BCS theory. It is therefore urgent to discover more candidates with spin-triplet superconductivity.

Several Cr-based superconductors have been reported to show unconventional superconductivity. For Cr-based compounds, superconductivity was first discovered by applying external pressure in CrAs, which is on the verge of antiferromagnetic order<sup>26,27</sup>. Nuclear quadrupole resonance (NQR) measurements reveal that substantial magnetic fluctuations are present in CrAs, and the absence of coherence peak in relaxation rate below  $T_c$  indicates an unconventional pairing mechanism<sup>28</sup>. Further

neutron scattering measurements of CrAs<sup>29,30</sup> support a direct connection between magnetism and superconductivity.  $\text{A}_2\text{Cr}_3\text{As}_3$  ( $A = \text{Na}, \text{K}, \text{Rb},$  and  $\text{Cs}$ )<sup>31–33</sup> have also attracted much interest. The existence of nodes in the superconducting gap is evidenced by the transport and muon spin relaxation ( $\mu\text{SR}$ ) measurements<sup>34,35</sup>. The presence of strong ferromagnetic spin fluctuations is revealed by <sup>75</sup>As nuclear magnetic resonance (NMR) measurements<sup>36</sup> and NQR<sup>37</sup> measurements. Therefore, a possible  $p$ -wave superconducting state was suggested in  $\text{A}_2\text{Cr}_3\text{As}_3$ <sup>38,39</sup>.

Recently, the first Cr-based nitride superconductor  $\text{Pr}_3\text{Cr}_{10-x}\text{N}_{11}$  with  $T_c = 5.25$  K was discovered<sup>40</sup>. The upper critical field  $H_{c2}(0)$  of  $\text{Pr}_3\text{Cr}_{10-x}\text{N}_{11}$  is  $\sim 12.6$  T, which is much larger than the estimated Pauli paramagnetic pair-breaking magnetic field. The correlation between  $3d$  electrons derived from specific heat data is ten times larger than that estimated by the electronic structure calculation<sup>40</sup>. The enhanced correlation may be induced by the quantum fluctuations<sup>41,42</sup>. However, the study of the superconducting pairing symmetry is still lacking.

We report detailed muon spin relaxation ( $\mu\text{SR}$ ) and specific heat measurements of the polycrystalline sample of  $\text{Pr}_3\text{Cr}_{10-x}\text{N}_{11}$ . Although the specific heat coefficient  $\gamma = C_e/T$  in the superconducting state down to 0.5 K is best described by a full gap model,  $C_e/T \propto e^{-\Delta_0/(k_B T)}$ ,  $\Delta_0/k_B T_c$  is only  $\sim 1.19(3)$ . This is much smaller than the weak coupling limit BCS value 1.76. Intriguingly, a large value of  $\gamma(0)$  is discovered, and the field dependence of  $\gamma_0(H)$  resembles that of the U-based ferromagnetic superconductors  $\text{UTe}_2$

<sup>1</sup>State Key Laboratory of Surface Physics and Department of Physics, Fudan University, Shanghai, China. <sup>2</sup>ISIS Facility, STFC Rutherford Appleton Laboratory, Harwell Science and Innovation Campus, Didcot, Oxfordshire, UK. <sup>3</sup>Department of Physics, University of Zurich, Zurich, Switzerland. <sup>4</sup>Beijing National Laboratory for Condensed Matter Physics and Institute of Physics, Chinese Academy of Sciences, Beijing, China. <sup>5</sup>School of Physical Sciences, University of Chinese Academy of Sciences, Beijing, China. <sup>6</sup>Songshan Lake Materials Laboratory, Dongguan, Guangdong, China. <sup>7</sup>Collaborative Innovation Center of Advanced Microstructures, Nanjing University, Nanjing, China. <sup>8</sup>Shanghai Research Center for Quantum Sciences, Shanghai, China. ✉ e-mail: [welyman@iphy.ac.cn](mailto:welyman@iphy.ac.cn); [leishu@fudan.edu.cn](mailto:leishu@fudan.edu.cn)

and URhGe. It is worth mentioning that  $\text{UTe}_2$  does not have any long-range ferromagnetic order, and URhGe has a ferromagnetic phase. Thus, the “ferromagnetic” here is a broad definition. The temperature dependence of superfluid density measured by transverse-field (TF)  $\mu\text{SR}$  down to 0.3 K is consistent with a  $p$ -wave pairing symmetry. Furthermore, the zero-field (ZF)  $\mu\text{SR}$  experiment reveals the spontaneous appearance of an internal magnetic field below  $T_c$ , indicating time-reversal symmetry breaking in the superconducting state. Meanwhile, the temperature-independent spin fluctuations at low temperatures are suggested by the longitudinal-field (LF)  $\mu\text{SR}$  experiments.

## Results and discussion

### Specific heat measurements

The specific heat coefficient  $C/T$  vs.  $T^2$  for  $\text{Pr}_3\text{Cr}_{10-x}\text{N}_{11}$  measured with different applied magnetic fields are shown in the inset of Fig. 1a. Sharp superconducting transitions can be seen. The field-independent normal state data are well fitted by  $C/T = \gamma_n + \beta T^2$ , yielding  $\gamma_n = 0.193(4) \text{ mJ g}^{-1} \text{ K}^{-2}$  and  $\beta = 1.61(3) \mu\text{J g}^{-1} \text{ K}^{-4}$ . With a rough estimation of  $x = 0.5$  (see Supplementary Data of ref. 40), we have a large value of  $\gamma_n$  per mole Cr  $\gamma_n = 21.8(1) \text{ mJ K}^{-2} \text{ mol-Cr}^{-1}$ . The large  $\gamma_n$  suggests strong correlations between electrons. Figure 1b shows  $H_{c2}(T)$  determined from specific heat measurements for  $\text{Pr}_3\text{Cr}_{10-x}\text{N}_{11}$ .  $H_{c2}(0) = 20 \text{ T}$  or  $31 \text{ T}$ , extrapolated by the fits using an empirical formula<sup>40</sup>  $H_{c2}(T) = H_{c2}(0)(1 - (T/T_c)^2)$  or GL-model<sup>43</sup>, respectively, while the Pauli paramagnetic limit  $H_p = 1.84 T_c$  is only  $\sim 9.6 \text{ T}$ . This suggests that the superconductivity of  $\text{Pr}_3\text{Cr}_{10-x}\text{N}_{11}$  is unlikely to have conventional  $s$ -wave pairing symmetry.

By subtracting the phonon contribution  $\beta T^2$ , the temperature dependencies of  $C_e/(T\gamma_n)$  at different applied magnetic fields are obtained and displayed in Fig. 1a. Interestingly,  $C_e/T$  in the superconducting states for different applied magnetic fields can still be described by a full gap model<sup>44,45</sup>  $C_e/T \propto e^{-\Delta_0/(k_B T)}$  with  $\Delta_0 = 0.54 \text{ meV}$ . We notice that  $\Delta_0/k_B T_c$  is only  $\sim 1.19(3)$ , which is much smaller than the weak coupling limit BCS value 1.76. It is worth mentioning that point nodes in the energy gap are easy to be erased by the mixing of electrons with different orbital angular momentum:  $l \neq l_0$  ( $l_0 = 1$  for  $p$ -wave pairing system, and the mixing electrons can come from any itinerant electrons with orbital angular momentum  $l \neq 1$ )<sup>46</sup>. In this case,  $C_e/T$  is still exponential at low temperatures for a

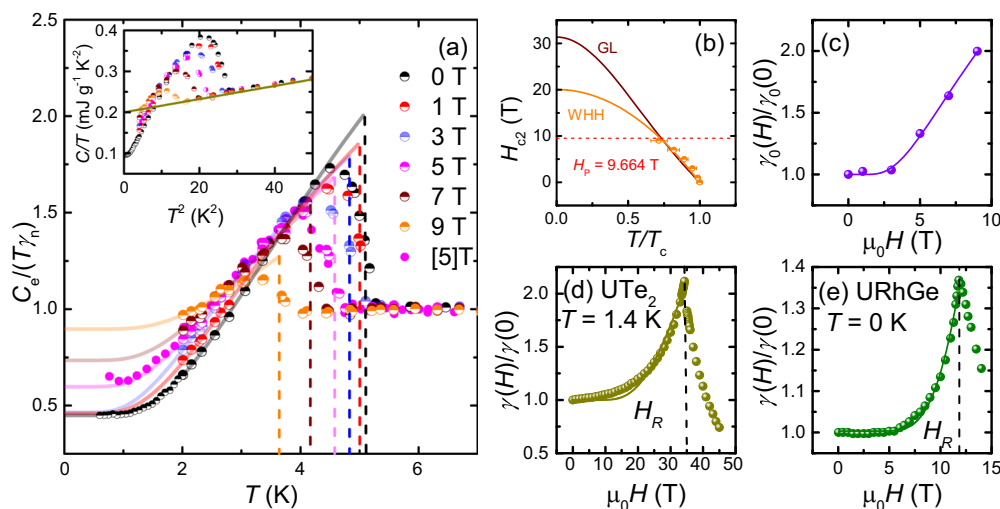
full-gap superconductor, but  $\Delta_0/(k_B T_c)$  is smaller than the BCS value of 1.43 at  $T_c$ . This is consistent with our zero-field-specific heat measurement, which gives  $\Delta_0/(k_B T_c) = 1.0(1)$ .

By applying magnetic fields,  $C/T$  shows an increase at low temperatures (shown by magenta solid dots in Fig. 1a). This can be due to a hyperfine-enhanced  $\text{Pr}^{3+}$  nuclear Schottky anomaly which was commonly reported in Pr systems<sup>47–49</sup>, and can not be deducted easily. By extrapolating the fitting curves of full-gap model to  $T = 0 \text{ K}$  with entropy balance  $\int_0^{T_c(H)} C_e/T dT = \gamma_n T_c(H)$  imposed, we obtain the field dependence of residual coefficient  $\gamma_0(H)$  (Fig. 1c). The fitted gap value  $\Delta_0$  slightly decreases with increasing fields, suggesting a large critical magnetic field  $H_{c2}$ . In the clean limit, the zero temperature  $\gamma_0$  of an  $s$ -wave superconductor is  $\gamma_0 \sim 0$ . Impurity phase would contribute nonzero  $\gamma_0$  in the dirty limit, but  $\gamma_0(H)$  should be field-independent in this case. For  $d$ -wave or  $p$ -wave superconductivity,  $\gamma_0 \neq 0$  due to the nodes in the superconducting gap, and  $\gamma_0(H)$  changes with  $\sqrt{H}$  for line nodes<sup>50</sup>. However,  $\gamma_0(H)$  of  $\text{Pr}_3\text{Cr}_{10-x}\text{N}_{11}$  is not consistent with any case mentioned above, but is well described by an exponential function  $[\gamma_0(H) - \gamma_0(0)]/\gamma_n = e^{-H^*/H}$ , as shown in Fig. 1c. Similar exponential dependence of low-temperature  $\gamma$  was also found in ferromagnetic superconductors  $\text{UTe}_2$ <sup>19</sup> and URhGe<sup>51</sup>, which are considered to hold spin-triplet superconductivity. In these U-based single crystals, the enhanced Sommerfeld coefficient is due to the enhancement of ferromagnetic (FM) fluctuations when approaching the FM instability. The possible origin of the exponential-like increment  $\gamma_0(H)$  in  $\text{Pr}_3\text{Cr}_{10-x}\text{N}_{11}$  could be the field-enhanced anisotropic gap structure<sup>52</sup>, or the field-enhanced unpaired electrons correlation<sup>18,53</sup>.

### TF- $\mu\text{SR}$ experiments

To further probe the superconducting gap symmetry of  $\text{Pr}_3\text{Cr}_{10-x}\text{N}_{11}$ , TF- $\mu\text{SR}$  experiments have been performed. Figure 2a shows the asymmetry spectra in an applied field of 50 mT at  $T = 0.3 \text{ K}$  (vortex state) and  $T = 8 \text{ K}$  (normal state). Faster damping is observed at base temperature compared to the normal state data. The data are fitted well by the following function form:

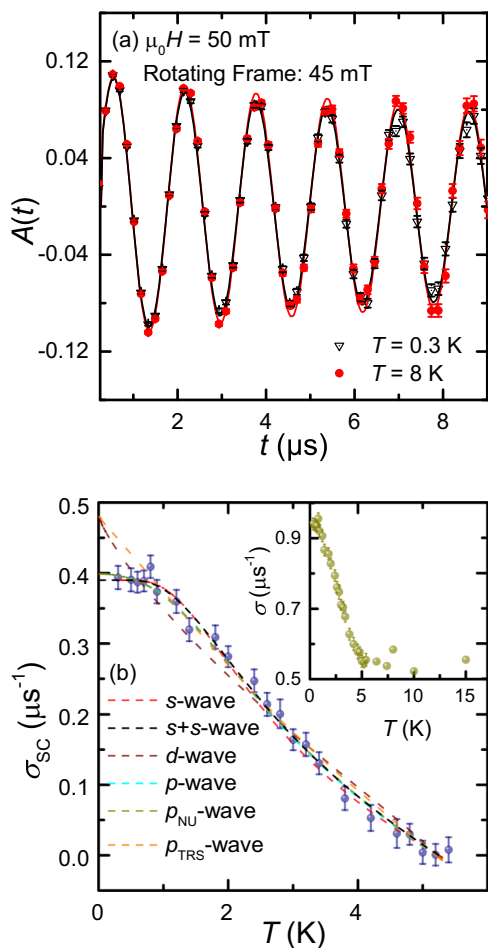
$$A(t) = \sum_{i=1}^2 A_i e^{-\frac{1}{2}\sigma_i^2 t^2} \cos(\gamma_i B_i t + \varphi_i) + A_b \cos(\gamma_b B_b t + \varphi_b), \quad (1)$$



**Fig. 1 | Specific heat data of  $\text{Pr}_3\text{Cr}_{10-x}\text{N}_{11}$  under different magnetic fields.**

**a** Temperature dependence of electronic specific heat coefficient  $C_e/(T\gamma_n)$  with different applied magnetic fields are presented in different colors:  $\mu_0 H = 0 \text{ T}$  (black),  $\mu_0 H = 1 \text{ T}$  (red),  $\mu_0 H = 3 \text{ T}$  (blue),  $\mu_0 H = 5 \text{ T}$  (magenta),  $\mu_0 H = 7 \text{ T}$  (wine),  $\mu_0 H = 9 \text{ T}$  (orange). The solid lines are the fits with full-gap-model. The dashed lines indicate  $T_c$  for different fields, determined by the middle of the jump. It is worth mentioning that the magenta full-solid dots were measured on an additional sample. To show the difference, the data were named as [5] T. Inset:  $C/T$  vs.  $T^2$  for different applied fields.

The solid line is the fit of the normal state data. **b** Temperature dependence of  $H_{c2}$  determined from specific heat measurements are shown in orange. Solid lines are the fits of WWH and GL-model (see the text). Dashed line: the Pauli paramagnetic limit. The error bars represent the estimated uncertainty for  $T_c$  under corresponding magnetic fields. **c–e** Sommerfeld coefficient  $\gamma(H)$  of  $\text{Pr}_3\text{Cr}_{10-x}\text{N}_{11}$  (indicated by purple dots),  $\text{UTe}_2$  (indicated by dark-yellow dots)<sup>19</sup>, and URhGe (indicated by olive dots)<sup>51</sup>. Solid lines: fits of  $\gamma_0(H)/\gamma_0(0) \sim e^{-H^*/H}$ .



**Fig. 2 | TF-μSR asymmetry spectra and data analysis with various models for Pr<sub>3</sub>Cr<sub>10-x</sub>N<sub>11</sub>.** **a** Representative TF-μSR asymmetry spectra for Pr<sub>3</sub>Cr<sub>10-x</sub>N<sub>11</sub> in the normal (circles) and superconducting (triangles) states with an external magnetic field of  $\mu_0 H_{\text{ext}} = 50$  mT. Solid curves are the fits to the data with Eq. (1). For clarity, the spectra are shown in a rotating reference frame corresponding to a field of 45 mT. **a** Error bars indicate the statistical error. **b** Temperature dependence of muon spin relaxation rate  $\sigma_{\text{sc}}$ , the lines are the fits to Eq. (4) with five different models, and the fitting parameters are listed in Table 1. Inset: Temperature dependence of muon spin relaxation rate  $\sigma$  determined by Eq. (2). **b** Error bars are obtained from the fitted equations described in the main text.

where the first and second terms correspond to muons that stop in the sample and silver sample holder, respectively. The silver background signal is temperature-independent, and  $A_1$  and  $A_2$  are also temperature-independent, even above  $T_c$ . The second moment of the composite field distribution in the sample can be calculated as<sup>54</sup>:

$$(\sigma/\gamma_\mu)^2 = \sum_{i=1}^2 \frac{A_i}{A_1 + A_2} [(\sigma_i/\gamma_\mu)^2 - [B_i - \langle B \rangle]^2], \quad (2)$$

where

$$\langle B \rangle = \sum_{i=1}^2 \frac{A_i B_i}{A_1 + A_2}. \quad (3)$$

The relaxation rate induced by vortex lattice can be extracted by  $\sigma_{\text{sc}} = [\sigma^2 - \sigma_{\text{nm}}^2]^{\frac{1}{2}}$ , where  $\sigma_{\text{nm}}$  is originated from nuclear dipole moments, which is temperature-independent and determined at  $T > T_c$ . The temperature dependence of  $\sigma_{\text{sc}}$  is plotted in Fig. 2b. Since the applied field  $\mu_0 H_a = 50 \text{ mT} \ll H_{c2}$ , the penetration depth  $\lambda_L$  in vortex state has a relation with the second moment of the inner field distribution<sup>55,56</sup>:

$(\sigma_{\text{sc}}/\gamma_\mu)^2 = \Delta B^2 = 0.00371 \frac{\Phi_0^2}{\lambda_L^4}$ , where  $\gamma_\mu = 2\pi \times 135.5 \text{ MHz T}^{-1}$  is the muon gyromagnetic ratio,  $\Phi_0 = 2.07 \times 10^{-15} \text{ Wb}$  is the magnetic-flux quantum, and the magnetic penetration depth  $\lambda_L$  is related to the superfluid density  $n_s$  and effective mass of electron  $m^*$  by the London equation  $1/\lambda_L^2 = 4\pi n_s e^2 / m^* c^2$ . Considering the situation for the full-gap model or point nodes model, we have  $\sigma_{\text{sc}}(0 \text{ K}) \sim 0.403 \mu\text{s}^{-1}$ . Then, we can derive  $\lambda_L = 516(3) \text{ nm}$ . The small difference in  $A(t)$  above and below  $T_c$  is attributed to the large penetration depth  $\lambda_L$ , which is consistent with the observation of large  $\gamma^{40}$ . The normalized superfluid density  $n_s(T)/n_s(0) = \sigma_{\text{sc}}(T)/\sigma_{\text{sc}}(0)$  is obtained and plotted in Fig. 2b. The temperature dependence of  $\sigma_{\text{sc}}(T)/\sigma_{\text{sc}}(0)$  can be fitted by following function<sup>57-59</sup>:

$$\frac{\sigma_{\text{sc}}(T)}{\sigma_{\text{sc}}(0)} = 1 + \frac{1}{2\pi} \int_0^{2\pi} \int_0^\pi \int_{\Delta(T, \varphi, \theta)}^\infty \left( \frac{\partial f}{\partial E} \right) \frac{E \sin \theta dE d\varphi d\theta}{\sqrt{E^2 - \Delta(T, \varphi, \theta)^2}}, \quad (4)$$

where

$$f = [1 + \exp(E/k_B T)]^{-1}, \quad (5a)$$

$$\Delta(T, \varphi, \theta) = \Delta_0 \delta \left( \frac{T}{T_c} \right) g(\varphi, \theta), \quad (5b)$$

$$\delta \left( \frac{T}{T_c} \right) = \tanh \left\{ 1.82 \left[ 1.018 \left( \frac{T_c}{T} - 1 \right) \right]^{0.51} \right\}. \quad (5c)$$

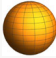
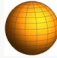
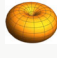

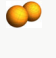

$\Delta_0$  is the maximum superconducting energy gap value at  $T = 0 \text{ K}$ ,  $f$  is the Fermi function,  $k_B$  is the Boltzmann constant,  $g(\varphi, \theta)$  describes the angular dependence of the gap, and  $\varphi$  and  $\theta$  are the angular coordinates in  $k$ -space. It is worth noting that Eq. (4) is applied for three-dimensional situation, since Pr<sub>3</sub>Cr<sub>10-x</sub>N<sub>11</sub> has a typical three-dimensional cubic structure.

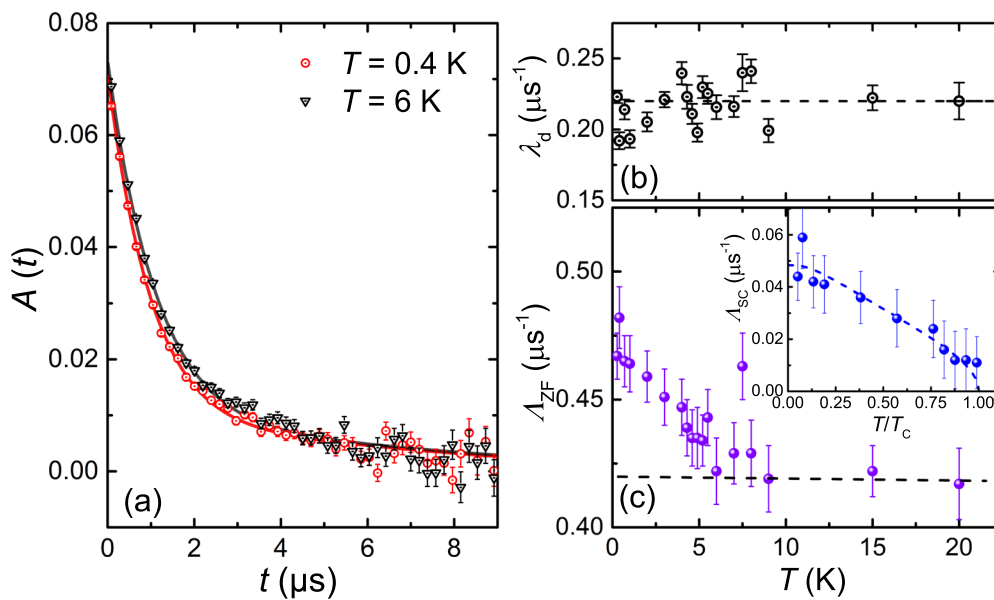
During the fitting procedure, a traditional  $s$ -wave superconductivity with  $g(\varphi, \theta) = 1$  ( $s$ -wave, red points), a two-gap structure fitted with  $\alpha$  model<sup>58</sup> ( $s + s$ -wave, black points), a unitary  $p$ -wave state  $k_x \pm ik_y$ , with  $g(\varphi, \theta) = |\sin \theta|$  ( $p$ -wave, cyan points), a  $p$ -wave state  $k_x$  which conserve the time-reversal-symmetry (TRS) with  $g(\varphi, \theta) = |\sin \theta \cos \varphi|$  ( $p_{\text{TRS}}$ -wave, orange points), a nonunitary  $p$ -wave gap structure with  $g(\varphi, \theta) = \text{NU}(\theta, \varphi) = a|\sin \theta \cos \varphi + \sin \theta \sin \varphi| + (1 - a)|\sin \theta \cos \varphi - \sin \theta \sin \varphi|$  ( $p_{\text{NU}}$ -wave, dark-yellow points), and a  $d_{x^2-y^2}$  gap structure were considered ( $d$ -wave, wine points). The fitting parameters are listed in Table 1. We find that the normalized superfluid density of Pr<sub>3</sub>Cr<sub>10-x</sub>N<sub>11</sub> can be well described by both the  $s$ -wave model and  $p$ -wave model. However, for the  $s$ -wave model,  $\Delta_0^s/k_B T_c = 1.02(3)$ , which is much smaller than the BCS value of 1.76. This is reflected in the very narrow plateau of low-temperature superfluid density as shown in Fig. 2b, which is not consistent with conventional isotropic superconductivity<sup>60,61</sup>. The two-gap model with  $s + s$  gives a similar small gap value for the dominant gap, and an extremely small gap with large uncertainty. This suggests that the second gap is not necessary to better describe the data. As can be seen from Fig. 2b and Table 1,  $p$ -wave model with point nodes in the gap function not only describes the data well but also gives reasonable gap values. Another possibility is the anisotropic  $s$ -wave superconductivity, which would result in a smaller superconducting gap. However, it is worth mentioning that Eq. (2)<sup>54</sup> is applicable to single-quanta vortex lattice, while the vortex lattice in  $p$ -wave superconductors can be very different<sup>62</sup>.

### ZF- and LF-μSR experiments

ZF-μSR is a powerful method to detect the spontaneous but extremely small internal magnetic field in the superconducting state, which is evidence of TRS breaking<sup>63-67</sup>. Figure 3a shows representative μSR asymmetry spectra measured in ZF for Pr<sub>3</sub>Cr<sub>10-x</sub>N<sub>11</sub>, above and below  $T_c$ . A non-relaxing background signal originating from muons that miss the sample and stop in the silver sample holder has been subtracted. The absence of early-time oscillations or fast relaxation excludes the existence of strong static magnetism. However, the small additional relaxation below  $T_c$  can be seen.

**Table 1 | Fitting parameters for different gap symmetry models**

Model	$s$	$s + s$	$p_x \pm ip_y$	$\tilde{x}p_x + i\tilde{y}p_y$	$p_x$	$d_{x^2-y^2}$
$g(\varphi)$	1	1	$ \sin \theta $	$NU(\theta, \varphi)$	$ \sin \theta \cos \varphi $	$ \sin^2 \theta \cos 2\varphi $
$\Delta_0$	0.46(1) meV	0.52(3) (80%) 0.2(1) (20%)	0.59(1) meV	0.67(3) meV	0.85(1) meV	0.990(3) meV
$\Delta_0/k_B T_c$	1.02(3)	1.19(4) 0.46(9)	1.30(4)	1.5(2)	1.88(5)	2.18(1)
Nodes	\	\	Point	Point	Line	Line
TRS	Conserved	Conserved	Broken	Broken	Conserved	Surface state broken bulk state conserved
$\chi^2$	0.663	0.618	0.676	0.775	1.73	1.98
Plot						



**Fig. 3 | Evidence for time-reversal symmetry breaking by ZF-μSR data.**  
**a** Representative ZF asymmetry spectra for Pr<sub>3</sub>Cr<sub>10-x</sub>N<sub>11</sub>, measured above and below T<sub>c</sub> (triangles and circles, respectively). A constant background signal has been subtracted from the data. Solid curves: fits using the damped Lorentzian KT function Eq. (6). **a** Error bars indicate the statistical error. **b** Temperature dependence of the

exponentially damping rate λ<sub>d</sub>. The dashed line is the guide of the eye. **c** Temperature dependence of ZF KT static Lorentzian relaxation rate Λ<sub>ZF</sub> with λ<sub>d</sub> is fixed at 0.22 μs<sup>-1</sup>. Inset: temperature dependence of electronic relaxation rate Λ<sub>SC</sub> (see text). Blue dashed line: fit using Eq. (7). **b, c** Error bars are obtained from the fitted equation Eq. (6).

The ZF asymmetry time spectra A(t) over the whole measured temperature range are best described by the exponentially damped Lorentzian Kubo–Toyabe (KT) function plus a background signal from the silver sample holder:

$$A(t) = A_s \left[ \frac{1}{3} + \frac{2}{3} (1 - \Lambda_{ZF} t) e^{-\Lambda_{ZF} t} \right] e^{-\lambda_d t} + A_b, \quad (6)$$

where A<sub>s</sub> is the initial asymmetry for the sample signal, A<sub>b</sub> is the background signal which is temperature-independent and originated from muons stopping in the sample holder. The expression in brackets is the Lorentzian KT function, which represents a Lorentzian distribution inner field. In general, the field distribution of internal fields such as nuclear dipole moments is Gaussian-like shape<sup>68</sup>. In Pr<sub>3</sub>Cr<sub>10-x</sub>N<sub>11</sub>, there are different muon-stopping sites inside the sample, as indicated by the TF-μSR experiments. The superposition of the independent Gaussian distributions due to different muon sites is approximated to be a Lorentzian distribution. The same origin for the Lorentzian nuclear field distribution has also been reported in La<sub>4</sub>Ni<sub>3</sub>O<sub>8</sub><sup>69</sup> and Sr<sub>2</sub>Ir<sub>0.9</sub>Rh<sub>0.1</sub>O<sub>4</sub><sup>70</sup>. The damping rate λ<sub>d</sub> is often interpreted as a

dynamic relaxation rate usually originating from spin fluctuations. The temperature dependence of λ<sub>d</sub> is shown in Fig. 3b. Within error bars, λ<sub>d</sub> is constant around 0.22 μs<sup>-1</sup>. Such spin fluctuations may be responsible for the enhanced electron correlations observed in the specific heat measurements<sup>41,42</sup>.

Figure 3c shows the temperature dependence of Λ<sub>ZF</sub> with λ<sub>d</sub> fixed at 0.22 μs<sup>-1</sup>. Above T<sub>c</sub> Λ<sub>ZF</sub> is temperature-independent, as expected for muon depolarization by quasi-static nuclear moments<sup>68</sup>. It is worth mentioning that the large value of Λ<sub>n</sub> and σ<sub>nm</sub> above T<sub>c</sub> might be induced by hyperfine-enhanced Pr<sup>3+</sup> nuclear moments<sup>71</sup>. Below T<sub>c</sub> Λ<sub>ZF</sub> has a significant increase due to the onset of static local fields, which is evidence for broken TRS<sup>4,72</sup>. The increase is of electronic origin, so the electronic and random nuclear contributions (Λ<sub>SC</sub> and Λ<sub>n</sub>, respectively) are uncorrelated and added in Λ<sub>ZF</sub>(T) = Λ<sub>SC</sub>(T) + Λ<sub>n</sub>. In the inset of Fig. 3c, Λ<sub>SC</sub>(T) is plotted as a function of normalized temperature T/T<sub>c</sub>. The data can be fitted with the approximate empirical expression<sup>73,74</sup>

$$\Lambda_{SC}(T) = \Lambda_{SC}(0) \tanh \left[ b \sqrt{\frac{T_c}{T} - 1} \right], \quad (7)$$

assuming that  $\Lambda_{SC}$  has the temperature dependence of a BCS-like order parameter. The values of the fitting parameters are listed in Table 2. The zero temperature  $\Lambda_{SC}(0)$  is  $\sim 0.042(5) \mu\text{s}^{-1}$ , corresponding to the enhanced field  $\Lambda_{SC}(0)/\gamma_{\mu} = 0.49(5) \text{ G}$ . It is interesting to note that a similar magnitude of enhanced relaxation rate was reported in  $\text{Sr}_2\text{RuO}_4$ <sup>3,75</sup> and  $\text{Lu}_5\text{Rh}_6\text{Sn}_{18}$ <sup>76</sup>. The coefficient  $b = 0.95(5)$  is much smaller than 1.74 for an isotropic BCS superconductor in the weak coupling limit. This indicates a relatively weak electron–phonon coupling strength<sup>77</sup>, therefore the large upper critical field  $H_{c2}$  is not likely induced by the strong coupling effect. Alternatively,  $\Lambda_{SC}$  is attributed to other mechanisms besides BCS theory.

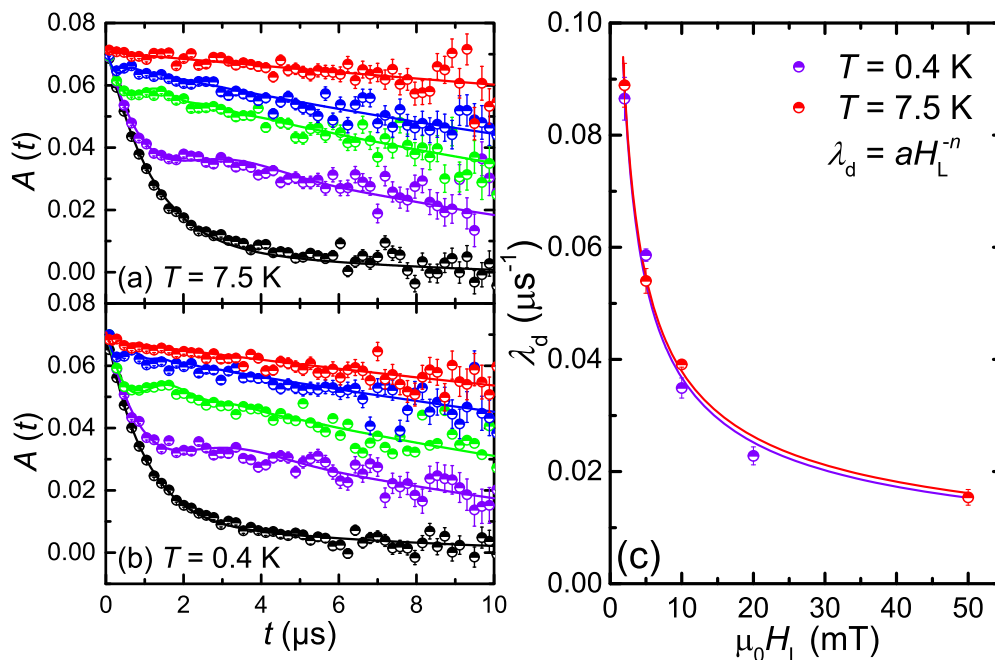
It is noted that the static and dynamic field contributions to the muon spin relaxation rate are hard to disentangle experimentally at zero-field. For LF- $\mu\text{SR}$  measurements, where the applied magnetic field  $H_L$  is parallel to the initial muon spin polarization, and  $H_L$  is much greater than static local fields at muon sites, the muon spin polarization is “decoupled” from the static local fields, and any remaining relaxation for high  $H_L$  is dynamic in origin<sup>78</sup>. LF- $\mu\text{SR}$  experiments were carried out in both the superconducting state at  $T = 0.4 \text{ K}$  and normal state at  $T = 7.5 \text{ K}$ . The asymmetry spectra are shown in Fig. 4a, b. The field dependence of  $A(t)$  shows characteristics of both decoupling and field-dependent dynamic relaxation: the small-amplitude oscillation with frequency  $\omega_L$  at small fields is a feature of decoupling<sup>68</sup>, but decoupling alone would not account for the nonzero field dependence of the overall relaxation rate.

The data are well-fitted using the following equation

$$A(t) = A_s P_Z^{\text{LF,LKT}}(B_{\text{ext}}, \Lambda) e^{-\lambda_d t} + A_b, \quad (8)$$

**Table 2 | Parameters from fit of Eq. (7)**

$\Lambda_{SC}(0)$	$0.042(5) \mu\text{s}^{-1}$
$\Lambda_{SC}(0)/\gamma_{\mu}$	$0.49(5) \text{ G}$
$b$	$0.95(5)$
$T_c$	$5.5(3) \text{ K}$



**Fig. 4 | Temperature-independent fluctuations indicated by LF- $\mu\text{SR}$  data.** **a, b** LF asymmetry spectra for  $\text{Pr}_3\text{Cr}_{10-x}\text{N}_{11}$  for  $T = 7.5 \text{ K}$  (**a**),  $T = 0.4 \text{ K}$  (**b**). A constant background signal has been subtracted from the data. Curves: Fits of Eq. (8) to the spectra. **a, b** Error bars indicate the statistical error. **c** Field dependence of dynamical

where  $P_Z^{\text{LF,LKT}}(B_{\text{ext}}, \Lambda)$  is the depolarization function for a Lorentz field distribution of static local fields in an applied uniform magnetic field  $B_{\text{ext}}$ <sup>68</sup>,  $\Lambda/\gamma_{\mu}$  is the half-width at half-maximum of the field distribution, which is field-independent and was fixed at the value of  $\Lambda_{ZF}(T)$ . The field dependence of dynamical rate  $\lambda_d$  in Fig. 4c are well described as  $\lambda_d(H_L) = aH_L^{-n}$ , where  $a = 0.45(8)$ ,  $n = 0.54(5)$  for  $T = 0.4 \text{ K}$ , and  $a = 0.43(4)$ ,  $n = 0.53(1)$  for  $T = 7.5 \text{ K}$ . The power-law behaviors of  $\lambda_d(H)$  can be interpreted as a signature of low-energy spin dynamics<sup>79</sup>. The overlapping of  $\lambda_d(H)$  curves, i.e., same fitting parameters  $a$  and  $n$  within error bars, for  $T = 0.4 \text{ K}$  and  $T = 7.5 \text{ K}$  indicates that  $\lambda_d$  has the same field dependence at different temperatures and confirms the temperature-independent behavior of  $\lambda_d$  observed in ZF- $\mu\text{SR}$  experiment. Thus the enhanced relaxation  $\Lambda_{ZF}$  below  $T_c$  is due to the static magnetism.

In summary, specific heat measurements reveal a large  $H_{c2}$  value and a large  $\gamma(0)$  of  $\text{Pr}_3\text{Cr}_{10-x}\text{N}_{11}$ , which is consistent with our former report<sup>40</sup>. A power-law behavior of the field dependence of  $\gamma_0(H)$  resembles that of the U-based ferromagnetic superconductors  $\text{UTe}_2$  and  $\text{URhGe}$ . This needs to be confirmed by the measurements on higher-quality samples, since it was found that  $\gamma_0(0)$  has sample dependence for  $\text{UTe}_2$  single crystals<sup>80</sup>. Although the temperature dependence of specific heat is described by a full-gap model  $C_e/T \propto e^{-\Delta_0/(k_B T)}$ , a small value of  $\Delta_0 = 0.54 \text{ meV}$  is obtained. This might be explained by either there is an anisotropic full gap, or the possibility that point nodes in the energy gap are easy to be erased by the mixing of electrons with different orbital angular momentum. Temperature dependence of superfluid density measured by TF- $\mu\text{SR}$  measurements can be described by both unitary  $p$ -wave model:  $p_x \pm ip_y$ , and nonunitary  $p$ -wave model:  $\hat{x}p_x + i\hat{y}p_y$ , with gap values similar to the one obtained from specific heat measurements, anisotropic  $s$ -wave model can not be excluded either. ZF- $\mu\text{SR}$  experiment suggests a TRSB superconducting transition, and temperature-independent spin fluctuations at low temperatures are revealed by LF- $\mu\text{SR}$  experiments. Such spin fluctuations may be responsible for the enhanced electron correlations observed in the specific heat measurements<sup>41,42</sup>.

The results reveal that  $\text{Pr}_3\text{Cr}_{10-x}\text{N}_{11}$  is a candidate of  $p$ -wave superconductor which breaks time-reversal symmetry. However, only polycrystalline samples of  $\text{Pr}_3\text{Cr}_{10-x}\text{N}_{11}$  can be obtained so far. Higher-quality

muon spin relaxation rate  $\lambda_d$  at 7.5 K (red circles) and 0.4 K (purple circles) respectively. Curves: Fits of  $\lambda_d = aH_L^{-n}$ . The error bars are obtained from the fitted equation Eq. (8).

samples or single crystals are needed, and additional experimental probes are required to check whether superconductivity such as  $s + is$  or  $s + id$  is applicable.

## Methods

### Experimental methods

Polycrystalline samples of  $\text{Pr}_3\text{Cr}_{10-x}\text{N}_{11}$  were prepared by solid-state reaction, and the characterization data can be found in ref. <sup>40</sup>. Low-field magnetization measurements suggest that magnetic impurities are negligible in the sample. Specific heat measurements down to  $T = 2$  K and magnetic field up to  $\mu_0 H = 9$  T were performed in a Physical Property Measurement System using a standard thermal relaxation technique.  $\mu\text{SR}$  measurements were carried out on MuSR spectrometer at the ISIS Neutron and Muon Facility, Rutherford Appleton Laboratory, Chilton, UK, over the temperature range 0.27–20 K. About 1 g samples were glued to a silver holder covering a circle with 1 inch in diameter using dilute GE varnish. Stray fields at the sample position were canceled within 1  $\mu\text{T}$  in three directions.

### Data availability

All relevant data are available from the corresponding authors upon request. Part of the data is taken from refs. <sup>19</sup> and <sup>51</sup> with reuse permission. The  $\mu\text{SR}$  data were generated at ISIS (Neutron and Muon Facility, Rutherford Appleton Laboratory, UK). Derived data supporting the results of this study are available from the corresponding authors or beamline scientists. The Musrfit software package is available online free of charge at <https://lmu.web.psi.ch/musrfit/user/html/setup-standard.html>.

### Code availability

The methods for the numerically generated points and lines reported in the plots of this paper are described in the main text. The actual codes used to produce the results reported in this paper are available from the corresponding author upon request.

Received: 30 September 2023; Accepted: 13 February 2024;

Published online: 06 March 2024

## References

- Wilczek, F. Majorana returns. *Nat. Phys.* **5**, 614–618 (2009).
- Stern, A. Non-abelian states of matter. *Nature* **464**, 187–193 (2010).
- Luke, G. M. et al. Time-reversal symmetry-breaking superconductivity in  $\text{Sr}_2\text{RuO}_4$ . *Nature* **394**, 558–561 (1998).
- Mackenzie, A. P. & Maeno, Y. The superconductivity of  $\text{Sr}_2\text{RuO}_4$  and the physics of spin-triplet pairing. *Rev. Mod. Phys.* **75**, 657–712 (2003).
- Nelson, K. D., Mao, Z. Q., Maeno, Y. & Liu, Y. Odd-parity superconductivity in  $\text{Sr}_2\text{RuO}_4$ . *Science* **306**, 1151–1154 (2004).
- Ishida, K. et al. Spin-triplet superconductivity in  $\text{Sr}_2\text{RuO}_4$  identified by  $^{17}\text{O}$  Knight shift. *Nature* **396**, 658–660 (1998).
- Mackenzie, A. P., Scaffidi, T., Hicks, C. W. & Maeno, Y. Even odder after twenty-three years: the superconducting order parameter puzzle of  $\text{Sr}_2\text{RuO}_4$ . *NPJ Quantum Mater.* **2**, 40 (2017).
- Kim, B., Khmelevskiy, S., Mazin, I. I., Agterberg, D. F. & Franchini, C. Anisotropy of magnetic interactions and symmetry of the order parameter in unconventional superconductor  $\text{Sr}_2\text{RuO}_4$ . *NPJ Quantum Mater.* **2**, 37 (2017).
- Pustogow, A. et al. Constraints on the superconducting order parameter in  $\text{Sr}_2\text{RuO}_4$  from oxygen-17 nuclear magnetic resonance. *Nature* **574**, 72–75 (2019).
- Suh, H. G. et al. Stabilizing even-parity chiral superconductivity in  $\text{Sr}_2\text{RuO}_4$ . *Phys. Rev. Res.* **2**, 032023 (2020).
- Ishida, K., Manago, M., Kinjo, K. & Maeno, Y. Reduction of the  $^{17}\text{O}$  Knight shift in the superconducting state and the heat-up effect by NMR pulses on  $\text{Sr}_2\text{RuO}_4$ . *J. Phys. Soc. Jpn.* **89**, 034712 (2020).
- Petsch, A. N. et al. Reduction of the spin susceptibility in the superconducting state of  $\text{Sr}_2\text{RuO}_4$  observed by polarized neutron scattering. *Phys. Rev. Lett.* **125**, 217004 (2020).
- Joynt, R. & Taillefer, L. The superconducting phases of  $\text{UPt}_3$ . *Rev. Mod. Phys.* **74**, 235–294 (2002).
- Tou, H. et al. Odd-parity superconductivity with parallel spin pairing in  $\text{UPt}_3$ : evidence from  $^{195}\text{Pt}$  Knight shift study. *Phys. Rev. Lett.* **77**, 1374–1377 (1996).
- Fisher, R. A. et al. Specific heat of  $\text{UPt}_3$ : evidence for unconventional superconductivity. *Phys. Rev. Lett.* **62**, 1411–1414 (1989).
- Schöttli, S. et al. Evidence for unconventional superconductivity in  $\text{UPt}_3$  from magnetic torque studies. *Phys. Rev. B* **62**, 4124–4131 (2000).
- Lambert, F., Akbari, A., Thalmeier, P. & Eremin, I. Surface state tunneling signatures in the two-component superconductor  $\text{UPt}_3$ . *Phys. Rev. Lett.* **118**, 087004 (2017).
- Ran, S. et al. Nearly ferromagnetic spin-triplet superconductivity. *Science* **365**, 684–687 (2019).
- Aoki, D. et al. Unconventional superconductivity in  $\text{UTe}_2$ . *J. Phys. Condens. Matter* **34**, 243002 (2022).
- Nakamine, G. et al. Superconducting properties of heavy fermion  $\text{UTe}_2$  revealed by  $^{125}\text{Te}$ -nuclear magnetic resonance. *J. Phys. Soc. Jpn.* **88**, 113703 (2019).
- Metz, T. et al. Point-node gap structure of the spin-triplet superconductor  $\text{UTe}_2$ . *Phys. Rev. B* **100**, 220504 (2019).
- Kittaka, S. et al. Orientation of point nodes and nonunitary triplet pairing tuned by the easy-axis magnetization in  $\text{UTe}_2$ . *Phys. Rev. Res.* **2**, 032014 (2020).
- Bae, S. et al. Anomalous normal fluid response in a chiral superconductor  $\text{UTe}_2$ . *Nat. Commun.* **12**, 2644 (2021).
- Hayes, I. M. et al. Multicomponent superconducting order parameter in  $\text{UTe}_2$ . *Science* **373**, 797–801 (2021).
- Wei, D. S. et al. Interplay between magnetism and superconductivity in  $\text{UTe}_2$ . *Phys. Rev. B* **105**, 024521 (2022).
- Wu, W. et al. Superconductivity in the vicinity of antiferromagnetic order in CrAs. *Nat. Commun.* **5**, 5508 (2014).
- Kotegawa, H., Nakahara, S., Tou, H. & Sugawara, H. Superconductivity of 2.2 K under pressure in helimagnet CrAs. *J. Phys. Soc. Jpn.* **83**, 093702 (2014).
- Kotegawa, H. et al. Detection of an unconventional superconducting phase in the vicinity of the strong first-order magnetic transition in CrAs using  $^{75}\text{As}$ -nuclear quadrupole resonance. *Phys. Rev. Lett.* **114**, 117002 (2015).
- Keller, L. et al. Pressure dependence of the magnetic order in CrAs: a neutron diffraction investigation. *Phys. Rev. B* **91**, 020409 (2015).
- Matsuda, M. et al. Evolution of magnetic double helix and quantum criticality near a dome of superconductivity in CrAs. *Phys. Rev. X* **8**, 031017 (2018).
- Bao, J.-K. et al. Superconductivity in quasi-one-dimensional  $\text{K}_2\text{Cr}_3\text{As}_3$  with significant electron correlations. *Phys. Rev. X* **5**, 011013 (2015).
- Tang, Z.-T. et al. Superconductivity in quasi-one-dimensional  $\text{Cs}_2\text{Cr}_3\text{As}_3$  with large interchain distance. *Sci. China Mater.* **58**, 16–20 (2015).
- Tang, Z.-T. et al. Unconventional superconductivity in quasi-one-dimensional  $\text{Rb}_2\text{Cr}_3\text{As}_3$ . *Phys. Rev. B* **91**, 020506 (2015).
- Shao, Y. T. et al. Evidence of line nodes in superconducting gap function in  $\text{K}_2\text{Cr}_3\text{As}_3$  from specific-heat measurements. *EPL* **123**, 57001 (2018).
- Adroja, D. T. et al. Superconducting ground state of quasi-one-dimensional  $\text{K}_2\text{Cr}_3\text{As}_3$  investigated using  $\mu\text{SR}$  measurements. *Phys. Rev. B* **92**, 134505 (2015).
- Zhi, H. Z., Imai, T., Ning, F. L., Bao, J.-K. & Cao, G.-H. Nmr investigation of the quasi-one-dimensional superconductor  $\text{K}_2\text{Cr}_3\text{As}_3$ . *Phys. Rev. Lett.* **114**, 147004 (2015).

37. Yang, J., Tang, Z. T., Cao, G. H. & Zheng, G.-Q. Ferromagnetic spin fluctuation and unconventional superconductivity in  $\text{Rb}_2\text{Cr}_3\text{As}_3$  revealed by  $^{75}\text{As}$  NMR and NQR. *Phys. Rev. Lett.* **115**, 147002 (2015).
38. Luo, J. et al. Tuning the distance to a possible ferromagnetic quantum critical point in  $\text{A}_2\text{Cr}_3\text{As}_3$ . *Phys. Rev. Lett.* **123**, 047001 (2019).
39. Yang, J. et al. Spin-triplet superconductivity in  $\text{K}_2\text{Cr}_3\text{As}_3$ . *Sci. Adv.* **7**, eabl4432 (2021).
40. Wu, W. et al. Superconductivity in chromium nitrides  $\text{Pr}_3\text{Cr}_{10-x}\text{N}_{11}$  with strong electron correlations. *Natl Sci. Rev.* **7**, 21–26 (2019).
41. Miyake, A. et al. Enhancement and discontinuity of effective mass through the first-order metamagnetic transition in  $\text{UTe}_2$ . *J. Phys. Soc. Jpn.* **90**, 103702 (2021).
42. Zou, Y. et al. Fermi liquid breakdown and evidence for superconductivity in  $\text{YFe}_2\text{Ge}_2$ . *Phys. Status Solidi Rapid Res. Lett.* **8**, 928–930 (2014).
43. Zhu, X., Yang, H., Fang, L., Mu, G. & Wen, H.-H. Upper critical field, hall effect and magnetoresistance in the iron-based layered superconductor  $\text{LaFeAsO}_{0.9}\text{F}_{0.1-\delta}$ . *Supercond. Sci. Technol.* **21**, 105001 (2008).
44. Singh, D. et al. Time-reversal symmetry breaking in the noncentrosymmetric superconductor  $\text{Re}_6\text{Ti}$ . *Phys. Rev. B* **97**, 100505 (2018).
45. Singh, D., Sajjesh, K. P., Marik, S., Hillier, A. D. & Singh, R. P. Superconducting and normal state properties of the noncentrosymmetric superconductor  $\text{NbOs}_2$  investigated by muon spin relaxation and rotation. *Phys. Rev. B* **99**, 014516 (2019).
46. Leggett, A. J. A theoretical description of the new phases of liquid  $^3\text{He}$ . *Rev. Mod. Phys.* **47**, 331–414 (1975).
47. Aoki, Y. et al. Thermodynamical study on the heavy-fermion superconductor  $\text{PrOs}_4\text{Sb}_{12}$ : evidence for field-induced phase transition. *J. Phys. Soc. Jpn.* **71**, 2098–2101 (2002).
48. Pathak, A. K., Paudyal, D., Mudryk, Y., Gschneidner, K. A. & Pecharsky, V. K. Anomalous Schottky specific heat and structural distortion in ferromagnetic  $\text{PrAl}_2$ . *Phys. Rev. Lett.* **110**, 186405 (2013).
49. Hargreaves, T. et al. Low-temperature specific heat of the electron-doped superconductor  $\text{Pr}_{2-x}\text{Ce}_x\text{CuO}_{4-\delta}$ . *Phys. C* **303**, 33–40 (1998).
50. Kopnin, N. B. & Volovik, G. E. Flux flow in  $d$ -wave superconductors: low temperature universality and scaling. *Phys. Rev. Lett.* **79**, 1377–1380 (1997).
51. Hardy, F. et al. Transverse and longitudinal magnetic-field responses in the Ising ferromagnets  $\text{URhGe}$ ,  $\text{UCoGe}$ , and  $\text{UGe}_2$ . *Phys. Rev. B* **83**, 195107 (2011).
52. Anand, V. K. et al. Specific heat and  $\mu\text{SR}$  study on the noncentrosymmetric superconductor  $\text{LaRhSi}_3$ . *Phys. Rev. B* **83**, 064522 (2011).
53. Jiao, L. et al. Chiral superconductivity in heavy-fermion metal  $\text{UTe}_2$ . *Nature* **579**, 523–527 (2020).
54. Khasanov, R. et al. Muon-spin-rotation measurements of the penetration depth in  $\text{Li}_2\text{Pd}_3\text{B}$ . *Phys. Rev. B* **73**, 214528 (2006).
55. Brandt, E. H. Flux distribution and penetration depth measured by muon spin rotation in high- $T_c$  superconductors. *Phys. Rev. B* **37**, 2349–2352 (1988).
56. MacLaughlin, D. E. et al. Muon spin relaxation and isotropic pairing in superconducting  $\text{PrOs}_4\text{Sb}_{12}$ . *Phys. Rev. Lett.* **89**, 157001 (2002).
57. Maisuradze, A. et al. Superfluid density and energy gap function of superconducting  $\text{PrPt}_4\text{Ge}_{12}$ . *Phys. Rev. Lett.* **103**, 147002 (2009).
58. Khasanov, R. et al. Evidence of nodeless superconductivity in  $\text{FeSe}_{0.85}$  from a muon-spin-rotation study of the in-plane magnetic penetration depth. *Phys. Rev. B* **78**, 220510 (2008).
59. Shan, L. et al. Distinct pairing symmetries in  $\text{Nd}_{1.85}\text{Ce}_{0.15}\text{CuO}_{4-y}$  and  $\text{La}_{1.89}\text{Sr}_{0.11}\text{CuO}_4$  single crystals: evidence from comparative tunneling measurements. *Phys. Rev. B* **72**, 144506 (2005).
60. Biswas, P. K. et al. Chiral singlet superconductivity in the weakly correlated metal  $\text{LaPt}_3\text{P}$ . *Nat. Commun.* **12**, 2504 (2021).
61. Iguchi, Y. et al. Microscopic imaging homogeneous and single phase superfluid density in  $\text{UTe}_2$ . *Phys. Rev. Lett.* **130**, 196003 (2023).
62. Garaud, J., Babaev, E., Bojesen, T. A. & Sudbø, A. Lattices of double-quanta vortices and chirality inversion in  $p_x + ip_y$  superconductors. *Phys. Rev. B* **94**, 104509 (2016).
63. Aoki, Y. et al. Time-reversal symmetry-breaking superconductivity in heavy-fermion  $\text{PrOs}_4\text{Sb}_{12}$  detected by muon-spin relaxation. *Phys. Rev. Lett.* **91**, 067003 (2003).
64. Luke, G. M. et al. Muon spin relaxation in  $\text{UPt}_3$ . *Phys. Rev. Lett.* **71**, 1466–1469 (1993).
65. Hillier, A. D., Quintanilla, J. & Cywinski, R. Evidence for time-reversal symmetry breaking in the noncentrosymmetric superconductor  $\text{LaNiC}_2$ . *Phys. Rev. Lett.* **102**, 117007 (2009).
66. Biswas, P. K. et al. Evidence for superconductivity with broken time-reversal symmetry in locally noncentrosymmetric  $\text{SrPtAs}$ . *Phys. Rev. B* **87**, 180503 (2013).
67. Hillier, A. D. et al. Muon spin spectroscopy. *Nat. Rev. Methods Prim.* **2**, 4 (2022).
68. Hayano, R. S. et al. Zero- and low-field spin relaxation studied by positive muons. *Phys. Rev. B* **20**, 850–859 (1979).
69. Bernal, O. O. et al. Charge-stripe order, antiferromagnetism, and spin dynamics in the cuprate-analog nickelate  $\text{La}_4\text{Ni}_3\text{O}_8$ . *Phys. Rev. B* **100**, 125142 (2019).
70. Tan, C. et al. Slow magnetic fluctuations and critical slowing down in  $\text{Sr}_2\text{Ir}_{1-x}\text{Rh}_x\text{O}_4$ . *Phys. Rev. B* **101**, 195108 (2020).
71. MacLaughlin, D. E. et al. Weak quasistatic magnetism in the frustrated kondo lattice  $\text{Pr}_2\text{Ir}_2\text{O}_7$ . *Phys. B: Condens. Matter* **404**, 667–670 (2009).
72. Sigrist, M. & Ueda, K. Phenomenological theory of unconventional superconductivity. *Rev. Mod. Phys.* **63**, 239–311 (1991).
73. Zhang, J. et al. Broken time-reversal symmetry in superconducting  $\text{Pr}_{1-x}\text{La}_x\text{Pt}_4\text{Ge}_{12}$ . *Phys. Rev. B* **100**, 024508 (2019).
74. Gross, F. et al. Anomalous temperature dependence of the magnetic field penetration depth in superconducting  $\text{UBe}_{13}$ . *Z. Phys. B: Condens. Matter* **64**, 175–188 (1986).
75. Hicks, C. W. et al. Limits on superconductivity-related magnetization in  $\text{Sr}_2\text{RuO}_4$  and  $\text{PrOs}_4\text{Sb}_{12}$  from scanning squid microscopy. *Phys. Rev. B* **81**, 214501 (2010).
76. Bhattacharyya, A. et al. Broken time-reversal symmetry probed by muon spin relaxation in the caged type superconductor  $\text{Lu}_5\text{Rh}_6\text{Sn}_{18}$ . *Phys. Rev. B* **91**, 060503 (2015).
77. Coombes, J. M. & Carbotte, J. P. Dependence of  $2\Delta_0/k_B T_c$  on the shape of electron-phonon spectral density. *J. Low. Temp. Phys.* **63**, 431–446 (1986).
78. Blundell, S. J. Spin-polarized muons in condensed matter physics. *Contemp. Phys.* **40**, 175–192 (1999).
79. Keren, A., Mendels, P., Campbell, I. A. & Lord, J. Probing the spin-spin dynamical autocorrelation function in a spin glass above  $T_g$  via muon spin relaxation. *Phys. Rev. Lett.* **77**, 1386 (1996).
80. Aoki, D. et al. First observation of the de Haas-van Alphen effect and fermi surfaces in the unconventional superconductor  $\text{UTe}_2$ . *J. Phys. Soc. Jpn.* **91**, 083704 (2022).

## Acknowledgements

We thank Prof. Douglas E. MacLaughlin for the fruitful discussion. We are very grateful to the ISIS Cryogenics Group for valuable help during the  $\mu\text{SR}$  experiments (ISIS.RB 1910277). This research was supported by the National Key Research and Development Program of China, Nos. 2022YFA1402203 and 2021YFA1401800, the National Natural Science Foundations of China, Nos. 12174065 and 12134018, and the Shanghai Municipal Science and Technology Major Project Grant No. 2019SHZDX01. J.C. acknowledges support by the Swiss National Science

Foundation (Projects No. 200021-188564). C.S.C. acknowledges support by the China Scholarship Council.

### Author contributions

L.S. designed the experiments. W.W. and J.L.L. grew the samples. C.S.C., Z.H.Z., Y.X.Y., C.T., and A.D.H. performed the  $\mu$ SR experiments. Specific heat measurements were performed by C.S.C., Q.W., and M.Y.Z., C.S.C., and L.S. analyzed the data. All authors participated in the discussion. The manuscript was written by C.S.C., J.C., and L.S.

### Competing interests

The authors declare no competing interests.

### Additional information

**Correspondence** and requests for materials should be addressed to W. Wu or L. Shu.

**Reprints and permissions information** is available at <http://www.nature.com/reprints>

**Publisher's note** Springer Nature remains neutral with regard to jurisdictional claims in published maps and institutional affiliations.

**Open Access** This article is licensed under a Creative Commons Attribution 4.0 International License, which permits use, sharing, adaptation, distribution and reproduction in any medium or format, as long as you give appropriate credit to the original author(s) and the source, provide a link to the Creative Commons licence, and indicate if changes were made. The images or other third party material in this article are included in the article's Creative Commons licence, unless indicated otherwise in a credit line to the material. If material is not included in the article's Creative Commons licence and your intended use is not permitted by statutory regulation or exceeds the permitted use, you will need to obtain permission directly from the copyright holder. To view a copy of this licence, visit <http://creativecommons.org/licenses/by/4.0/>.

© The Author(s) 2024